Eur. J. Mech. B/Fluids 18 (1999) 823–846

Wall shear stress and void fraction in Poiseuille bubbly flows: Part I: simple analytic predictions

N. Rivière, A. Cartellier *

Laboratoire des Écoulements Géophysiques et Industriels—LEGI (INPG, CNRS, UJF), BP 53, 38041 Grenoble cedex, France

Abstract – Upward, co-current bubbly flows in a vertical rectangular duct are investigated at low liquid Reynolds numbers. The conditions considered are such that the pseudo-turbulent stresses remain negligible compared to the viscous stresses. The void fraction transverse distribution is idealised as step-functions and is then inserted in the conservation equations supplemented by appropriate closure laws. Analytical expressions are then obtained for the axial velocity profiles, for the lineic gas fraction and for the wall friction. The sensitivity of these quantities to the void distribution, characterised by the void fraction and the width of the three layers introduced, is discussed. It is shown that differential buoyancy effects govern the modification of the liquid velocity profiles. Notably, void peaking near walls is able to induce a wall shear stress many times higher than its single-phase flow counterpart at the same liquid flow rate. Also, the presence of a near wall region free of gas favours the onset of downward directed secondary flows. All these features correspond to experimental observations, and a few quantitative comparisons are also presented which support the validity of the model even in case of void coring. A companion paper (part II) will be devoted to systematic comparisons between predictions and experiments in the case of axisymmetric Poiseuille bubbly flows. © 1999 Éditions scientifiques et médicales Elsevier SAS

dispersed flows / void fraction distribution / Poiseuille bubbly flow / wall shear stress / two-fluid model / pseudo-turbulence

1. Introduction

The model presented here is intended to provide the wall shear stress and the gas fraction in vertical, upward co-current laminar bubbly flows. The denomination laminar holds while the liquid instability leading to shear-induced turbulence is not triggered. Therefore, the Reynolds stress reduces to the agitation induced by the dispersed phase.

Such slow flows of a liquid phase mixed with inclusions appear in various industrial applications. One can mention for instance their use in chemical reactors or contactors, or in separative techniques such as sedimentation or flotation devices. When the dispersed phase is not too dilute, or is not composed of too small inclusions, it does not passively follow the liquid, but has a strong interaction with the structure of the flow of the continuous phase. Indeed, experiments performed in laminar bubbly flows, i.e. in the absence of shear-induced turbulence, have shown that the presence of the dispersed phase can considerably modify the flow structure. For example, the flattening of the liquid velocity profiles has been observed in Poiseuille bubbly flows either in channels (Moechti Triyogi [1]; Cartellier et al. [2]) or in cylindrical ducts (Valukina et al. [3]; Sato et al. [4]; Nakoryakov et al. [5]; Kashinsky et al. [6]). By increasing the gas fraction, the liquid axial velocity can even become inverted near the walls. Such back flows have been identified many years ago in bubble columns where they are due to the buoyancy driven circulation of the initially stagnant liquid (see for example Rietema and Ottengraf [7]; Hills [8]), but they also exist in presence of an imposed liquid flow (Cartellier et al. [2,9]; Cartellier [10]). This is even true in strongly confined bubbly flows as recently shown by Kashinsky et al. [11].

* Correspondence and reprints

All these modifications have a profound influence on the wall shear stress, a fundamental quantity which is still hard to predict. Indeed, no complete prediction of laminar bubbly flows is available, even for confined conditions which are less complex than bubble columns for which the liquid circulation is one of the main unknowns (Celik and Wang [12]). For confined laminar bubbly flows, conservation equations of the Eulerian two-fluid model (Ishii [13]) supplemented by a coherent set of closure laws were presented by Achard and Cartellier [14] for the case of spherical bubbles at very high particulate Reynolds number. It was shown that void peaking is due to the action of a lift force of the type initially proposed by Zierep [15] (and which differs from the Saffman force) and of a wall repulsion force whose expression was left open. Besides, the pseudo-turbulent stress and the pressure disequilibrium at the interface, both evaluated from potential theory, were recognised to affect directly the transverse void distribution. Similar conclusions were later obtained for solid particles by Drew [16] and confirmed for bubbles by Antal et al. [17] who performed simulations after having supplemented the above approach with an expression for the wall repulsion force.

Despite these attempts, fundamental difficulties persist which preclude the establishment of a sound description of laminar bubbly flows. One of these is connected with the evaluation of forces acting on a bubble in a general confined flow field for any value of the particulate Reynolds number. Besides, the problem arises about how to express the interfacial momentum exchanges in near-wall regions or in the presence of a non-uniform spatial distribution of the dispersed phase. General expressions are also lacking for the pseudo-turbulence stress (and eventually for the interfacial disequilibrium introduced in some formulations), and for the so-called extra-deformation tensor which enters the average viscous stress tensor, not to mention the evaluation of the contribution of the fluctuating micro-scale motion of bubbles in the framework of the ‘classical’ two-fluid model. These drawbacks are of tremendous importance for the prediction of the dispersed phase transverse distribution because it is controlled by many weak effects. On the other hand, axial momentum exchanges involve strong mechanisms, much simpler to identify and to quantify.

In order to by-pass the above mentioned weaknesses, a part of the solution must be imposed. This simplified way to handle dispersed flows traces back, in its spirit, to one-dimensional models with an imposed kinematic, i.e. where the velocity profile of each phase is imposed (Wallis [18]; Zuber and Findlay [19]). However, only the shape of the void fraction profile, which is controlled by transverse effects, will be set out here. Such an approach has been used for bubble columns (Clark et al. [20]; Celik and Wang [12]), and it has been quite fruitful for the evaluation of wall shear stress in turbulent bubbly flows (Moursali et al. [21]; Marié et al. [22]). This approach was also the basis of a previous investigation of laminar bubbly flows (Cartellier et al. [9]); it requires two steps:

– by taking in consideration experimental profiles, a general void profile shape is retained;
– thanks to axial balance equations supplemented by appropriate closure laws, all other quantities are derived as a function of characteristic dimensionless parameters, using elementary analytical calculations. Notably, the lineic gas fraction and the liquid velocity profile are evaluated, and an explicit expression of the wall friction is obtained which illustrates the influence of the bubble distribution.

Besides, compared to our previous work (Cartellier et al. [9]), the void profile is more general and this feature, as we shall see, allows the capture of crucial aspects of the influence of the transverse bubble distribution on global quantities.

The paper is organised as follows: the class of dispersed flows considered is delineated and the corresponding balance equations for plane flows are given in sections 2.1 and 2.2 respectively. Starting from experimental findings, idealised void fraction profiles are then presented (section 2.3). When such profiles are introduced in the general balances, a solution is then obtained for the lineic gas fraction, the pressure drop, the velocity profile and the wall friction (section 2.4). Various limiting formulas are then derived, and the evolution of the

wall friction with the shape of the void fraction profile is discussed in section 3. A comparison with available data obtained in plane Poiseuille bubbly flows will support the validity of the approach.

2. Model with an imposed transverse void fraction profile

2.1. Class of flows investigated

In this paper, attention is focused on a sub-class of laminar bubbly flows, namely plane Poiseuille bubbly flows: ducts of constant section are considered, and the flows investigated are steady, (quasi) fully developed and parallel, i.e. without mean lateral or transverse velocities. The dispersed phase is composed of a monodispersion of spherical bubbles: this is a good approximation of some existing experiments in which the width of the size distribution does not exceed 20%. Besides, bubble interfaces are often contaminated and this feature must be taken into account when expressing the drag force. Last, the pressure conditions are far from the critical pressure so that the density and dynamic viscosity ratios ρ_G/ρ_L and μ_G/μ_L, where G and L refer to the gas and the liquid phase respectively, are much smaller than 1. Such flow conditions are characterised by six dimensionless parameters. The case investigated in this paper is that of a channel: its width is e in the transverse (y) direction and its extent is L in the lateral (x) direction, the axial or z direction is vertical and oriented upward. The corresponding set of dimensionless parameters is composed of:

– the Poiseuille number P, based on the flow rate per unit lateral length of the channel Q_L/L:

$$P = \frac{Q_L \mu_L}{\rho_L g L e^3} = \mathrm{Re}_L \frac{2\mu_L^2}{\rho_L^2 g e^3}, \tag{1}$$

where μ_L is the dynamic viscosity of the liquid phase and g is the gravity. As indicated in equation (1), the Poiseuille number is related to the liquid Reynolds number Re_L defined as $\rho_L Q_L/(2L\mu_L)$,

– the volumetric gas flow rate ratio involving the liquid Q_L and the gas Q_G flow rates:

$$\beta = \frac{Q_G}{Q_G + Q_L}; \tag{2}$$

– the dimensionless bubble radius $\varepsilon = d/2e$, where d is the bubble diameter;
– the aspect ratio of the channel $K = L/e$;
– the ratio $\kappa = (\mu_G + \xi)/\mu_L$ which characterises the contamination of interfaces, where ξ is a retardation coefficient (Newman [23]);
– the particulate Reynolds number Re_p defined as:

$$\mathrm{Re}_p = \frac{d w_r}{\nu_L} \tag{3}$$

which is connected to the mean relative velocity of bubbles $w_r = w_G - w_L$, where w_L and w_G are the phase averaged axial velocities (i.e. along the z direction) for the liquid and for the gas phase respectively.

Let us give some typical values of these dimensionless parameters. To ensure a laminar regime, P is at most O(1), and usually much less than 1. To maintain a dispersed regime, β must be less than 0.25 in usual fluids. Re_p ranges from unity up to few hundreds; it is mainly limited by the constraint on the sphericity of bubbles. Finally, ε is typically 0.01 and at most 0.1; such large values can be achieved notably with solid particles.

2.2. General conservation equations

In the framework of Eulerian two-fluids models (Ishii [13]), the conservation equations have been written for Poiseuille bubbly flows introducing general assumptions and scaling (Achard and Cartellier [14]). For parallel and two-dimensional flow fields, the phase averaged lateral (x-direction) and transverse velocities (along y) are zero, so that the continuity equations are identically satisfied. Thus, the system reduces to the phasic momentum balance equations, which can be written, following the model emitted by Ishii [13]:

$$\rho_k \alpha_k \left[\overline{v_k}^X \nabla\right] \overline{v_k}^X = -\alpha_k \nabla \overline{p_k}^X + \rho_k \alpha_k g + \nabla \cdot \left[\alpha_k \left(\overline{\tau_k}^X + \tau_k^T\right)\right] + \left[\overline{p_k}^i - \overline{p_k}^X + \overline{\tau_k^{nn}}^i\right] \nabla \alpha_k + M_k, \tag{4}$$

where the subscript $k = (\mathrm{L}, \mathrm{G})$ refers either to the liquid or the gas phase. The over bars indicate the average in the phase k, and are now dropped out for sake of simplicity. α_k represents the phase fraction. Let us briefly remember the significance of the last three terms involved in equation (4). The third term on the RHS involves the average viscous stress tensor τ_k^X, and the pseudo-turbulent stress tensor τ_k^T, due to the presence of inclusions. The fourth term in the RHS accounts for the pressure disequilibrium $p_k^i - p_k^X$ between the interface and the phase k, and of normal stresses at the interfaces τ_k^{nni}. Finally, equation (4) is supplemented by balance equations at the interface which make the relation $\underline{M}_\mathrm{G} = -\underline{M}_\mathrm{L}$ valid whenever the momentum sources due to curvature fluctuations and to surface tension gradients remain negligible. Interfacial balance allows also to connect the pressure levels in both phases: whatever the expression of the pressure disequilibrium $p_\mathrm{L}^i - p_\mathrm{L}^X$ as a function of the relative velocity, the fully developed assumption implies that the axial pressure gradients in both phases are identical. Hence, let us define the positive quantity G as:

$$\frac{\partial}{\partial z} p_\mathrm{L}^X = \frac{\partial}{\partial z} p_\mathrm{G}^X = -G. \tag{5}$$

Only the axial projections of equation (4) are required in our approach. Thus, by considering fully developed flows (section 2.1), the terms involving the void fraction gradients disappear. Similarly, with the full development assumption, the convective terms disappear for both phases. The smallness of the ratio $\rho_\mathrm{G}/\rho_\mathrm{L}$ and $\mu_\mathrm{G}/\mu_\mathrm{L}$ allows the neglect of the stress tensors and the gravity term in the momentum equation for the gas phase, which reduces to:

$$\alpha G = -M_\mathrm{G}^z = M_\mathrm{L}^z, \tag{6}$$

where α_G is noted α.

According to the classical procedure (Ishii and Zuber [24]) valid for homogeneous and steady suspensions, the interfacial momentum source along z is connected to the drag force F_z exerted by the liquid on a representative bubble according to:

$$M_\mathrm{L}^z = -\frac{6\alpha}{d} \frac{F_z}{\pi d^2} \tag{7}$$

in which:

$$F_z = -\frac{1}{2} C_\mathrm{D} \rho_\mathrm{L} \pi \frac{d^2}{4} w_\mathrm{r}^2. \tag{8}$$

For an isolated spherical bubble at low Weber number, C_D is well approximated by a $C_0/\mathrm{Re_p}$ law with a coefficient C_0 evolving with the bubble dynamics (namely high or low $\mathrm{Re_p}$) and with the contamination. For a bubble in a swarm, C_D becomes a function of the void fraction through the so-called hindering coefficient ϕ_1, which traduces the influence of the neighbouring bubbles on the dynamic of a representative bubble. The fact that the suspension is homogeneous corresponds to two main characteristics. Firstly, the bubbles are

monodispersed and have all the same dynamic given by the $\mathrm{Re_p}$. Then, their influence on the local liquid flow is the same. Secondly, it means that the bubbles are uniformly distributed in space. Hence, each representative bubble will experience the same influence from the neighbouring bubbles. In practice, we will consider, as the bubbles are monodispersed, that the suspension is homogeneous whenever the void fraction is uniform. Since in some expressions of ϕ_1 the effects of the void fraction and of the contamination are mixed (see section 3.1), the following form of the drag coefficient is considered:

$$C_\mathrm{D} = \frac{24\phi_1}{\mathrm{Re_p}}, \tag{9}$$

where the coefficient C_0 has been included in ϕ_1. A more realistic treatment would have taken into account the dependence of the drag coefficient with the distance to the wall. However, to be consistent, such a refinement has to be introduced into an expression of the interfacial momentum source valid in presence of strong void gradients and/or near walls (see section 2.3). Such expressions are available (Achard et al. [25]; Crispel et al. [26]) but they do not lead to formula in close form (instead, one needs detailed information on the number density and on the stress at the surface of bubbles at various distances from the wall). Therefore, to go on with analytical developments whose validity will be checked against experiments, no dependence of C_D with the distance to the wall is retained hereafter. The combination of equations (6)–(9) provides the final form of the axial momentum equation for the gas phase:

$$G = \frac{36\phi_1\mu_\mathrm{L}}{d^2} w_\mathrm{r} \tag{10}$$

which basically provides the relative axial velocity as a function of the imposed pressure gradient.

The liquid momentum equation projected along the z axis is written according to the above mentioned restrictions:

$$(1-\alpha)[\rho_\mathrm{L} g - G] = \frac{\partial}{\partial y}\left[(1-\alpha)\left(\tau_\mathrm{L}^{yzX} + \tau_\mathrm{L}^{yzT}\right)\right] + M_\mathrm{L}^z. \tag{11}$$

At this point, it is possible to derive an expression of the pressure drop valid for any steady flow in a duct of constant section. Indeed, eliminating the axial momentum source between equations (10) and (11), and integrating the resulting equation along the channel thickness provides the following relationship:

$$\mathrm{G} = \left(1 - \langle\alpha\rangle\right)\rho_\mathrm{L} g - 2\tau_\mathrm{w}/e, \tag{12}$$

where τ_w is the wall shear stress (here an algebraic quantity), and where the first term represents the weight of the two-phase column and involves the lineic gas fraction $\langle\alpha\rangle$ defined by:

$$\langle\alpha\rangle = \int_0^\mathrm{e} \alpha(y)\, dy/e. \tag{13}$$

Equation (12) will be used in section 2.4. Let us go back to equation (11) for which closure laws must be introduced for the average viscous stress tensor and for the pseudo-turbulent tensor.

For strongly contaminated bubbles, the stick condition holds on interfaces and the average viscous stress tensor is then given by the exact closure law first derived by Joseph and Lundgren [27] and confirmed using a different approach by Achard and Cartellier [28]. With the definition of the relative velocity, say $v_\mathrm{G}^X = v_\mathrm{L}^X + v_\mathrm{r}^X$, it can be written:

$$\tau_\mathrm{L}^X = 2\mu_\mathrm{L} D^\mathrm{S}\left[(1-\alpha)v_\mathrm{L}^X + \alpha v_\mathrm{G}^X\right] = 2\mu_\mathrm{L} D^\mathrm{S}\left[(1-\alpha)v_\mathrm{L}^X + \alpha v_\mathrm{L}^X + \alpha v_\mathrm{r}^X\right] = 2\mu_\mathrm{L} D^\mathrm{S}\left[v_\mathrm{L}^X + \alpha v_\mathrm{r}^X\right], \tag{14}$$

where the operator D^S is the symmetric part of the gradient. In the conditions considered here, one gets:

$$\tau_L^{yzX} = \mu_L \frac{d}{dy}\left[w_L^X + \alpha w_r^X\right]. \tag{15}$$

The usual way to model the viscous stress tensor is a rheological one which maintains the structure of the Newton closure but introduces a correction coefficient ϕ_0, a function of the local void fraction, namely:

$$\tau_L^X = 2\mu_L \phi_0(\alpha) D^S\left(v_L^X\right). \tag{16}$$

The contribution of the expression (16) to the axial liquid momentum reduces to:

$$\tau_L^{yzX} = \mu_L \phi_0(\alpha) \frac{d}{dy}\left[w_L^X\right]. \tag{17}$$

As we shall see in section 2.4, both closures are equivalent for the type of two-phase flows considered here when $\phi_0 = 1/(1-\alpha)$. Various forms for ϕ_0 are available in the literature: let us mention, among others, the famous Einstein–Taylor formula valid for vanishing $\mathrm{Re_p}$ and the work of Ryskin [29] who, in the dilute limit, has computed ϕ_0 for various $\mathrm{Re_p}$ and κ ratios: for clean bubbles at large $\mathrm{Re_p}$, he gets $\phi_0 = 1 + (5/3)\alpha$. At this stage, let us make two remarks. First, ϕ_1 and ϕ_0 are often not distinguished. The origin of this confusion relies probably in the fact that both functions can be crudely interpreted as an equivalent or effective viscosity of the mixture. However, their origin is fundamentally different, as demonstrated by the statistical theory of suspensions which predicts, for solid particles at very small $\mathrm{Re_p}$ and in the dilute limit, $\phi_0 = 1 + (5/2)\alpha$ and $\phi_1 = 1 + 6.5\alpha$. Second, great care must be exerted before using the available results, usually obtained from a mixture approach, in the framework of two-fluid models, because, in most cases, the expressions for ϕ_0 include a contribution from the extra deformation tensor and another one from the momentum exchange. For example, it has been shown that, in the case of the Einstein formula, these contributions are 1 and 3/2 respectively (Achard and Cartellier [30]).

The expression of the pseudo-turbulent tensor which arises in the liquid phase by the presence of bubbles is still an open question. The closure established by Nigmatulin [31] and Biesheuvel and van Wijngaarden [32], based on the accumulation of independent potential disturbances, leads to a diagonal stress tensor which, in the class of two-phase flows considered here, brings no contribution to the axial momentum balance. However, as shown by Cartellier et al. [33], this closure is no longer valid for small $\mathrm{Re_p}$ for which bubble-bubble interactions play an active role: the axial liquid velocity fluctuation $w_L'^2$ scales as $(\alpha/\mathrm{Re_p})w_r^2$ in the range $\alpha < 0.08$ and $0.8 < \mathrm{Re_p} < 30$ (with a prefactor still subject to discussions, see Cartellier et al. [34]). Assuming that this scaling is applicable to the transverse liquid velocity component, the yz component of the Reynolds stress, which is of relevance for the axial momentum equation for the liquid, scales at most as:

$$\tau_L^{yzT} = \mu_L \alpha w_r / d. \tag{18}$$

Hence, the ratio of the pseudo-turbulent stress to the viscous stress is given by:

$$\tau_L^{yzT} / \tau_L^{yzX} \approx \alpha (Y/d)(w_r/w_L) \approx \alpha (Y/d)^2 (\mathrm{Re_p}/\mathrm{Re_L}), \tag{19}$$

where Y is a typical length scale of the liquid phase velocity gradients. Near walls, Y is of the order of the bubble size d, so that the pseudo-turbulent stress is negligible compared to the viscous stress while the particulate Reynolds number is lower than the liquid Reynolds number (remember that α is less than 0.2). Far from the

walls, Y is of the order of the channel depth e and the same conclusion holds only if the particulate Reynolds number is much smaller than the liquid Reynolds number. Typically for 1 mm radius bubbles in a channel 10 cm wide, Re_p should not be higher than about one tenth Re_L. Such a condition is fulfilled in many available experimental data. Therefore, it is assumed that the pseudo-turbulent stress is everywhere negligible compared to the viscous tension. This important constraint defines the limit of validity of all the developments made in the following sections.

According to the above closures, the axial momentum balance equation for the liquid phase, once combined with equation (6), becomes:

$$(1-\alpha)\rho_L g - G = \frac{d}{dy}\left[(1-\alpha)\tau_L^{yzX}\right], \tag{20}$$

where the only remaining effect is connected with the average viscous stress in the liquid phase.

Up to this point, nothing has been imposed on the void profile. The next step consists of defining an idealised but realistic void profile and solving the above momentum balance for the liquid velocity profile.

2.3. The idealised transverse void profile

The simple model proposed now is inspired from the basic features of the transverse void fraction profiles observed in experiments. As illustrated in *figure 1*, the void fraction is usually almost constant in the centre of the channel, while large variations could occur near walls, in a region of typical extent a few bubbles sizes. Indeed, void peaking develops with the maximum of the void fraction located between 0.8 and 1.6 bubble diameter away from the wall, and with a typical extent of a few (1 to 3) bubble diameters. Let us recall that in turbulent conditions, this peak is usually located much closer to the walls, i.e. at about one bubble radius. Moreover, in laminar conditions, no gas phase is present in a near wall region whose extent is of the order of one bubble radius (this region is much thinner in turbulent flows). These features were observed in rectangular ducts (Cartellier et al. [9]; Moechti Triyogi [1]) and in tubes (Kashinsky and Timkin [35]). According to these

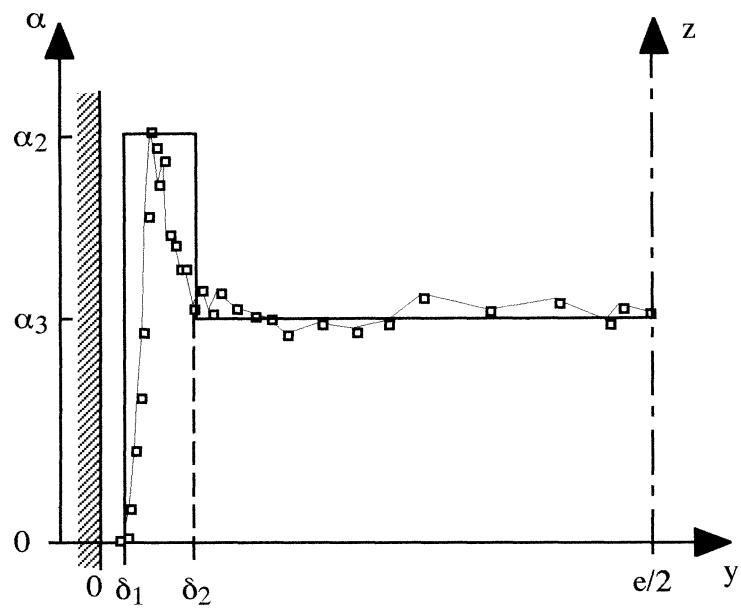

Figure 1. Typical experimental (open squares) and idealised (solid line) void fraction profiles.

observations, the following idealised phase structure is thus considered: the void fraction remains constant in the core of the channel ($y \geqslant \delta_2$), it is bounded by a higher constant void fraction corresponding to the void peaking region ($\delta_1 \leqslant y \leqslant \delta_2$) of width $\delta_2 - \delta_1$, leaving near the side walls a small gap of width δ_1 filled with the continuous phase alone ($y \leqslant \delta_1$). This step function structure, symmetrical with respect to the median plane $y = e/2$, is illustrated in *figure 1*.

2.4. Solution with the imposed void fraction

Introducing the idealised profile in the axial momentum equation for the liquid phase produces many simplifications. Equation (10) shows that the axial relative velocity w_r remains constant in each zone since the void fraction is constant. Therefore, equation (20) can be simplified to yield:

$$(1-\alpha)\rho_\mathrm{L} g - G = \begin{cases} \mu_\mathrm{L}\phi_0(1-\alpha)\dfrac{d^2 w_\mathrm{L}}{dy^2} & \text{Rheological closure,} \\ \mu_\mathrm{L}\dfrac{d^2 w_\mathrm{L}}{dy^2} & \text{Exact closure.} \end{cases} \tag{21}$$

From equation (21), it appears that a Newtonian law with a viscosity corrected by $\phi_0 = 1/(1-\alpha)$ gives the same result as the exact closure law for solids. Thus, the rheological form will be kept in the following since various closure proposals can enter in this frame. In the system composed of the equations (10) and (21), the unknowns are w_L and w_r (or G), while α is supposed as given. The first step of the resolution consists in solving for the liquid velocity profile. Equation (21) is written for each zone:

– for the single-phase flow zone 1 ($0 < y < \delta_1$):

$$\frac{d^2 w_\mathrm{L}^{(1)}}{dy^2} = [\rho_\mathrm{L} g - G]/\mu_\mathrm{L} \equiv s_1, \tag{22}$$

– for the two-phase flow zones 2 ($\delta_1 < y < \delta_2$) and 3 ($\delta_2 < y < e/2$):

$$\frac{d^2 w_\mathrm{L}^{(n)}}{dy^2} = \left[(1-\alpha_n)\rho_\mathrm{L} g - G\right] / \left[(1-\alpha_n)\mu_\mathrm{L}\phi_0^{(n)}\right] \equiv s_n, \quad n = 2 \text{ or } 3, \tag{23}$$

where $\phi_0^{(n)} = \phi_0(\alpha_n)$.

In equations (22) and (23), the parameters s_1, s_2 and s_3 are constants. Boundary conditions are

(i) zero liquid velocity at the walls,
(ii) symmetry with respect to the channel median plane, and at each boundary $y = \delta_1$ and $y = \delta_2$,
(iii) continuity of the tangential shear stress, and
(iv) continuity of the axial liquid velocity. The latter conditions express as:

$$\begin{gathered} w_\mathrm{L}^{(1)}(\delta_1) = w_\mathrm{L}^{(2)}(\delta_1) \quad \text{and} \quad w_\mathrm{L}^{(2)}(\delta_2) = w_\mathrm{L}^{(3)}(\delta_2), \\ \frac{dw_L^{(1)}}{dy}(\delta_1) = (1-\alpha_2)\phi_0^{(2)}\frac{dw_L^{(2)}}{dy}(\delta_1) \quad \text{and} \quad (1-\alpha_2)\phi_0^{(2)}\frac{dw_L^{(2)}}{dy}(\delta_2) = (1-\alpha_3)\phi_0^{(3)}\frac{dw_L^{(3)}}{dy}(\delta_2). \end{gathered} \tag{24}$$

Some elementary algebra provides the transverse liquid velocity profiles as a function of e, δ_1, δ_2, α_2, α_3, s_1, s_2, s_3, $\phi_0^{(2)}$ and $\phi_0^{(3)}$ (see the Appendix). The next step consists in expressing the constraints on global parameters

such as the liquid flow rate and the gas flow rate. Performing the integral of $(1-\alpha)w_{\mathrm{L}}$ over the channel thickness provides Q_{L} versus s_1, s_2 and s_3 which are known functions of the axial pressure gradient. Hence, G is obtained as a function of the Poiseuille number P according to:

$$\frac{G}{\rho_{\mathrm{L}} g} = (1-\alpha_3)\frac{N}{D} + \frac{12P\phi_0^{(3)}}{D}, \tag{25}$$

where N and D, which are given in the Appendix, are functions only of the characteristics of the void profile, namely α_2, α_3, and the dimensionless layer widths δ_1^*, δ_2^* defined as $\delta_n^* = \delta_n/e$ $(n = 1, 2)$.

2.4.1. Wall shear stress

The wall shear stress is obtained from the differentiation of the liquid velocity at walls or equivalently from the comparison of equation (12) with equation (25). Let us take into account the expression of the lineic gas fraction for the idealistic void fraction profile, which is written:

$$\langle\alpha\rangle = \alpha_3\left(1-2\delta_2^*\right) + 2\alpha_2\left(\delta_2^* - \delta_1^*\right) = \alpha_3\left[1-2\delta_1^*(a+b-ab)\right], \tag{26}$$

where the parameters a and b are defined as:

$$a = \delta_2/\delta_1 \quad \text{and} \quad b = \alpha_2/\alpha_3. \tag{27}$$

The parameter a is connected with the width $(\delta_2 - \delta_1)$ of the void peak scaled by the thickness δ_1 of the single-phase layer; a is always greater or equal to 1. The parameter b is the ratio of the void fraction at the peak to the void fraction in the core; it is always positive but not necessarily larger than one. One gets:

$$\begin{aligned}\frac{\tau_{\mathrm{w}}}{\tau_{\mathrm{w0}}} &= \frac{1}{12C_k P}\left[\frac{G}{\rho_{\mathrm{L}} g} - 1 + \langle\alpha\rangle\right] = \frac{\phi_0^{(3)}}{C_k D} + \frac{1}{12C_k P}\left[(1-\alpha_3)\left(\frac{N}{D}-1\right) + \langle\alpha\rangle - \alpha_3\right] \\ &= \frac{\phi_0^{(3)}}{C_k D} + \frac{1}{12C_k P}\left[(1-\alpha_3)\left(\frac{N}{D}-1\right) - 2\alpha_3\delta_1^*(a+b-ab)\right],\end{aligned} \tag{28}$$

where the two-phase flow wall friction τ_{w} has been scaled by the value of the wall shear stress τ_{w0} for the single-phase flow at the same liquid flow rate which is written:

$$\tau_{\mathrm{w0}} = -C_k 6P\rho_{\mathrm{L}} g e. \tag{29}$$

C_k is a coefficient function of the aspect ratio of the channel; it equals unity for a channel of infinite aspect ratio. Due to the two-dimensional character imposed on the two-phase flow, the expression of τ_{w} is strictly valid for an infinite aspect ratio. Hence, C_k is set to unity in the following for sake of consistency.

Equation (28) provides the wall shear stress as a function of the Poiseuille number, the aspect ratio and the parameters characterising the idealised void distribution, namely δ_1, a, α_3 and b. Since the latter quantities can be estimated from the measured void profile, the wall friction can be evaluated provided that the closure for ϕ_0 is known. The fact that the dimensionless bubble size ε, the particulate Reynolds number and the contamination do not appear explicitly in the expression of the wall friction should not be surprising. Indeed, these parameters control the absolute values of the void fraction and its transverse distribution and are thus implicitly included in the quantities δ_1, a, α_3 and b.

Equations (25) and (28) hold whatever the structure of the law chosen for ϕ_0. Since the interfaces are most often strongly contaminated, let us consider the exact closure equation (14) which, as mentioned in section 2.2, corresponds to $\phi_0 = 1/(1-\alpha)$. In this case, N and D are given by:

$$N = 1 - \frac{12\delta_1^{*2}}{1-\alpha_3}\left[\alpha_3(a^2-1)(b-1)\right] - \frac{8\delta_1^{*3}}{(1-\alpha_3)^2}\left[\alpha_3^2(a^3 - a^3b^2 + 3ab - 3a - 3ab^2 - 2b^2) + \alpha_3(a^3 - a^3b - 3a + b)\right], \tag{30a}$$

$$D = 1 - \frac{6\delta_1^{*2}}{1-\alpha_3}\left[\alpha_3(a^2-1)(b-1)\right] - \frac{4\delta_1^{*3}}{1-\alpha_3}\left[\alpha_3(a^3-1)(1-b)\right]. \tag{30b}$$

According to the experimental results discussed in section 2.3, the magnitude of δ_1 and of δ_2 are about one bubble diameter so that δ_1^* and δ_2^* are of the order of ε (and $a = \mathrm{O}(1)$). In the dispersed regime considered here, the bubble size is usually much smaller than the length scale of the base flow: ε is typically about 1% and at most equals 10%. Even if large values of the peak void fraction compared to the void fraction in the centre have been reported (i.e. b about 10 or more), it is legitimate to neglect all the terms connected with the void profile in equation (30). Since all the $\mathrm{O}(\varepsilon)$ contributions disappear with the closure chosen for ϕ_0, ones gets $N = D = 1 + \mathrm{O}(\varepsilon^2)$. Therefore, the ratio of shear stress in two-phase and in one-phase flow becomes

$$\frac{\tau_\mathrm{w}}{\tau_{\mathrm{w}0}} = \frac{1}{1-\alpha_3} - \frac{\langle\alpha\rangle - \alpha_3}{12P} + \mathrm{O}(\varepsilon^2) = \frac{1}{1-\alpha_3} - \frac{\alpha_3\delta_1^*}{6P}[a + b - ab] + \mathrm{O}(\varepsilon^2). \tag{31}$$

The first term in the R.H.S. of the above equation is due to the weighting factor affecting the liquid stress due to the presence of bubbles; it is always close to unity at least at low gas content. The second term is proportional to the difference between the lineic gas fraction and the void fraction in the core, meaning that any departure from a flat profile modifies the friction. This is clearly expressed by the terms inside brackets, which quantify the influence of the complete structure of the void fraction profile on the wall friction, and which illustrate the role of density differences between the layers. As we shall see in section 3, this second term has a drastic effect on the behaviour of the wall friction. The formula (31) can be rewritten as a function of the relative width of the void peaks, i.e. $(a-1)$ and of their intensity relative to the void in the core, i.e. $(b-1)$:

$$\frac{\tau_\mathrm{w}}{\tau_{\mathrm{w}0}} = \frac{1}{1-\alpha_3} + \frac{\alpha_3\delta_1^*}{6P}\left[(b-1)(a-1) - 1\right] + \mathrm{O}(\varepsilon^2). \tag{32}$$

It appears that the friction is controlled by α_3 which is close to the average gas fraction (see equation (26)), and by the dimensionless width of the single-phase layer δ_1^*. The other parameter affecting the wall shear stress is $(a-1)(b-1)$ which is proportional to the gas excess in the peak $(\delta_2 - \delta_1)(\alpha_2 - \alpha_3)$. A similar quantity was found to be of importance for bubbly turbulent boundary layers (Marié et al. [22]).

Equation (32) will be used in the sequel to analyse the behaviour of the wall shear stress with the structure of the void fraction profile. Before that, it is interesting to note that the ideal void distribution with wall peaking can be degenerated into a simpler structure namely, a flat void profile at the level α_3 with a monophasic layer of width δ_1. Indeed, wall peaks are eliminated by merely setting $b = 1$. In such conditions, ones recovers the simplified expression of the wall shear stress which has been previously derived (Cartellier et al. [9]). In that case, the pressure gradient is written:

$$\frac{G}{\rho_\mathrm{L} g} = 1 - \langle\alpha\rangle + \frac{12P}{1-\langle\alpha\rangle} + \mathrm{O}(\langle\alpha\rangle\varepsilon) + \mathrm{O}(\varepsilon^2) \tag{33}$$

and the wall friction obeys:

$$\frac{\tau_\mathrm{w}}{\tau_{\mathrm{w}0}} = \frac{1}{1-\alpha_3} - \frac{\alpha_3\delta_1^*}{6P} + \mathrm{O}(\varepsilon^2) = \frac{1}{1-\langle\alpha\rangle} - \frac{\langle\alpha\rangle\delta_1^*}{6P} + \mathrm{O}(\langle\alpha\rangle\varepsilon) + \mathrm{O}(\varepsilon^2), \tag{34}$$

where the last approximation results from equation (26). The result (34) provides an alternate interpretation of the complete formula (31). Indeed, the bracketed term in the RHS of (31) is composed of the sum of friction corrections due to three different degenerated profiles. The first term inside brackets represents the effect of a wall liquid layer of width $\delta_2 = a\delta_1$ with a central zone at a smaller density quantified by α_3 (*figure 2(a)*). The second bracketed term in equation (31), corresponds to a single phase layer of width δ_1 with a central zone of smaller density quantified by $\alpha_2 = b\alpha_3$ (*figure 2(b)*). These two-phase central zones increase the velocity in the core compared to a single-phase flow at the same liquid flow rate. Consequently, the velocity decreases near walls, and the wall shear stress is less than that of Poiseuille flow. The third term inside brackets has an opposite effect: it corresponds to a single-phase layer of width $\delta_2 = a\delta_1$ with an higher density central zone quantified by a negative void fraction of absolute value $\alpha_2 = b\alpha_3$ (*figure 2(c)*). Note that by adding the above degenerated profiles, the initial step function is recovered (*figure 2(d)*). In that last case, the velocity profile is flattened, and produces an increase of the wall friction compared to a single-phase situation. The intensity and the width of the void peak, or equivalently the gas excess in the peak compared to the core, determine which effect is the strongest. Therefore, wall shear stresses higher or lower than their single-phase counterpart can be obtained. This conclusion is valid because we choose as the reference wall friction in single-phase flow, its value obtained at the same liquid flow rate, the reason for that being that Q_L can be easily controlled during experiments. If single and two-phase conditions are compared with the same imposed pressure gradient G, the conclusion is different. Indeed, starting from equation (12) for single and two-phase situations, it is straightforward to show that:

$$\tau_w - \tau_{w0}^G = -2\rho_L g e \langle \alpha \rangle, \tag{35}$$

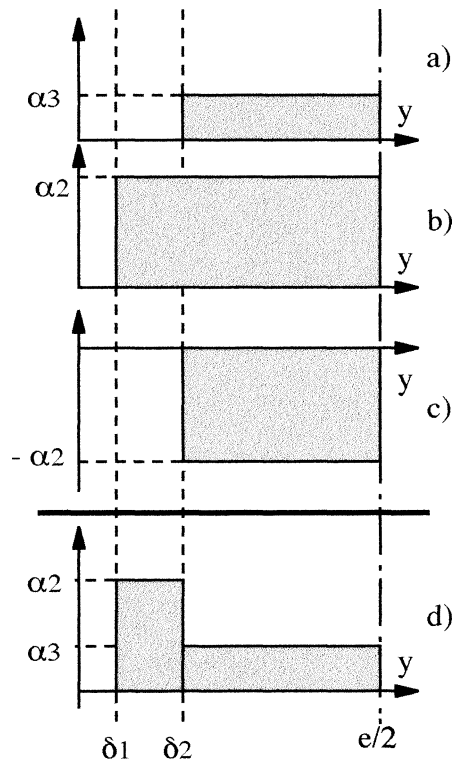

Figure 2. Decomposition of an idealised three layers void profile as the sum of two-layers void distributions.

where τ_{w0}^{G} is the wall shear stress in single-phase flow at the same G. Hence, the absolute value of the wall shear stress is always higher in two-phase conditions compared to single-phase one. This is simply due to the redistribution of the loss of weight toward the wall friction in equation (12).

2.4.2. Lineic gas fraction

A relationship between the void distribution and the characteristic parameters introduced in section 2.1 can be also derived. Indeed, let us express the second constraint, which corresponds to the evaluation of the gas flow rate. Integrating equation (10) over the channel thickness, and introducing Q_G, one gets:

$$\frac{\beta}{1-\beta} - \frac{\alpha_3}{1-\alpha_3} = \frac{4}{9}\frac{\varepsilon^2}{P}\frac{\alpha_3}{\phi_1(\alpha_3)}\frac{G}{\rho_L g}\left[\frac{1}{2} - a\delta_1^* + b(a-1)\delta_1^*\frac{\phi_1(\alpha_3)}{\phi_1(\alpha_2)}\right] + O(\varepsilon^2)$$
$$= \frac{2}{9}\frac{\varepsilon^2}{P}\frac{\alpha_3(1-\alpha_3)(N/D)}{\phi_1(\alpha_3)}\left[1 - 2a\delta_1^* + 2b(a-1)\delta_1^*\frac{\phi_1(\alpha_3)}{\phi_1(\alpha_2)}\right] + O(\varepsilon^2). \qquad (36)$$

The $O(\varepsilon^2)$ term in the first equality comes from an approximation of the liquid flow rate, while in the second equality, it includes also an approximation for the pressure gradient. In equation (36), the closure on viscous stresses is present from the ϕ_0 term included in the exact expressions of N and D (see the Appendix). However, since N and D are both equal to $1 + O(\varepsilon)$ whatever the law chosen for ϕ_0, this closure has a weak influence on the void level. On the other hand, the closure ϕ_1 is of primary importance; this is not surprising since ϕ_1 controls the relative velocity which produces the difference between β and the mean void fraction.

Since the parameters characterising the void profile appear in the above expression, it is not possible to estimate the lineic gas fraction from equation (36). However, equation (36) provides a means to identify the hindering function ϕ_1 from measurements of the void profile (this procedure was used by Cartellier et al. [9] with the degenerated model given hereafter). Equation (36) can reach a predictive status with respect to the gas fraction only if all the details of the void structure are eliminated. This occurs for the closure $\phi_0 = (1-\alpha)^{-1}$ when the monophasic layer is very thin (i.e. $\delta_1 \to 0$) provided that either the void peak disappears ($b = 1$) or its width is negligible (i.e. $a \to 1$): in these conditions, the equation (36) collapses into the following form which has been previously derived (Cartellier et al. [9]):

$$\frac{\beta}{1-\beta} - \frac{\alpha_3}{1-\alpha_3} = \frac{2}{9}\frac{\varepsilon^2}{P}\frac{\alpha_3(1-\alpha_3)}{\phi_1(\alpha_3)} + O(\delta_1^*), \qquad (37)$$

where α_3 can be equated to $\langle\alpha\rangle$ within an $O(\delta_1^*)$ approximation. The degenerated model is thus able to provide the lineic gas fraction ($\alpha_3 = \langle\alpha\rangle + O(\delta_1^*)$) versus the dimensionless parameters characteristic of the model provided that the hindering function ϕ_1 is known. Equation (37) can be interpreted as a Zuber and Findlay formula, but free of adjustable coefficients. Once α_3 has been obtained from equation (37), the wall shear stress can be evaluated using equation (34). Hence, the degenerated model provides all global quantities from the set of characteristic dimensionless parameters. On the other hand, for non-uniform void profiles, the determination of the void fraction transverse distribution is required to estimate the wall friction, so that this model is not fully predictive. As we shall see in the sequel where both approaches are compared, a non-uniform void profile is required to explain the experimentally observed behaviour of the wall friction.

3. Predicted behaviour and comparison with experiments

Before discussing the relationships established in the previous sections, let us briefly introduce the experimental conditions which will be used for comparison. Upward co-current, laminar bubbly flows have

been produced in a vertical rectangular channel such that $e = 60$ mm, $L = 500$ mm (see Moechti Triyogi [1]; Cartellier et al. [9] for details). The liquid is a mixture of tap water and glucose syrup ($\rho_L = 1220$ kg/m^3, $\nu_L = 28 \times 10^{-6}$ m^2/s, $\sigma = 0.0595$ N/m at 20°C). The Poiseuille numbers considered range from 4×10^{-5} to 4×10^{-4}, and β is less than 0.1. Air bubbles, injected 3 m upstream from the test section, are spherical and strongly contaminated ($\kappa = 6.27$). Their mean diameter is typically 1.2 mm, but it increases up to 2.0 mm for β about 0.08: hence ε is typically 0.01 and at most 0.02. The width of their size distribution is about ±17%. The particulate Reynolds number ranges from 1 to 2.5. The axial pressure gradient in the liquid G_L, connected to the averaged pressure gradient by $G_L = \rho_L g - G$, was measured (Moechti Triyogi [1]) in similar experiments ($9 \times 10^{-5} < P < 3 \times 10^{-4}$; $0.01 < \beta < 0.09$). It evolves linearity with the z coordinate, in a zone between 2 m upstream and 0.4 m downstream the test section, indicating that the flow was fully developed.

3.1. Lineic gas fraction

To analyse the behaviour of equation (36), an expression for the hindering coefficient ϕ_1 is required. After Zuber [36] and Ishii and Zuber [24], a rather general form is:

$$\phi_1(\alpha) = (1 - \alpha)^{-n}, \tag{38}$$

where the exponent n varies according to authors. For small inclusions, $n = 1$ seems reasonable for bubbles (Ishii and Zuber [24]), while for solids, n can be as high as 4.65 according to Richardson and Zaki [37]. A quite different closure, due to Gal-Or and Waslo [38] and valid for small particulate Reynolds numbers, mixes the void fraction and the contamination:

$$\phi_1(\alpha, \kappa) = \frac{1}{3} \frac{2(1 - \alpha^{5/3}) + (3 + 2\alpha^{5/3})\kappa}{(1 - \alpha^{1/3})(1 - \alpha^{5/3}) + \left(1 - \frac{3}{2}\alpha^{1/3} + \frac{3}{2}\alpha^{5/3} - \alpha^2\right)\kappa}. \tag{39}$$

For isolated bubbles ($\alpha = 0$), the equation (39) combined with equation (9) leads either to the Hadamard–Rybczynski drag for clean interfaces ($\kappa = 0$), or to the Stokes drag for solid particles ($\kappa = \infty$). For the above expressions for ϕ_1, the void fraction in the core as predicted by the degenerated model (equation (37)) is given *figure 3* for three typical values of ε^2/P. In the limit $\varepsilon^2/P \to 0$, i.e. when the relative velocity becomes negligible compared to the superficial liquid velocity, the solution of equation (37) is $\alpha = \beta$. However, in that case, $O(\delta_1^*)$ terms connected with the wall shear stress are no longer negligible compared to the ε^2/P contribution, and the model must be modified accordingly. For the laminar flows considered here, ε^2/P is always larger than the $O(\delta_1^*) = O(\varepsilon)$ terms. As shown in *figure 3*, the gas fraction becomes much lower than β as ε^2/P increases, i.e. as the relative velocity increases compared to the liquid superficial velocity. Besides, multiple solutions appear above a critical value of ε^2/P whatever the law chosen for ϕ_1. Since some of these solutions are unstable, this behaviour is possibly connected with flooding (Wallis [18]). The prediction of equation (37) combined with the Gal-Or and Waslo hindering function was shown to match very well the experimental findings for characteristics parameters in the range: $0 < \beta < 0.11$, $4 \times 10^{-5} < P < 4 \times 10^{-4}$, $0.01 < \varepsilon < 0.015$, $\kappa = 6.27$ and $1 < \mathrm{Re_p} < 10$ (Cartellier et al. [9]—these ranges have been obtained using an additional injector providing a mean bubble diameter of 2.2 mm).

3.2. Liquid velocity profiles and the onset of secondary flows

Another aspect of the model which could be tested concerns the velocity profiles, and the fact that downward directed secondary flows occur in the vicinity of walls provided that β is high enough (Cartellier et al. [9]).

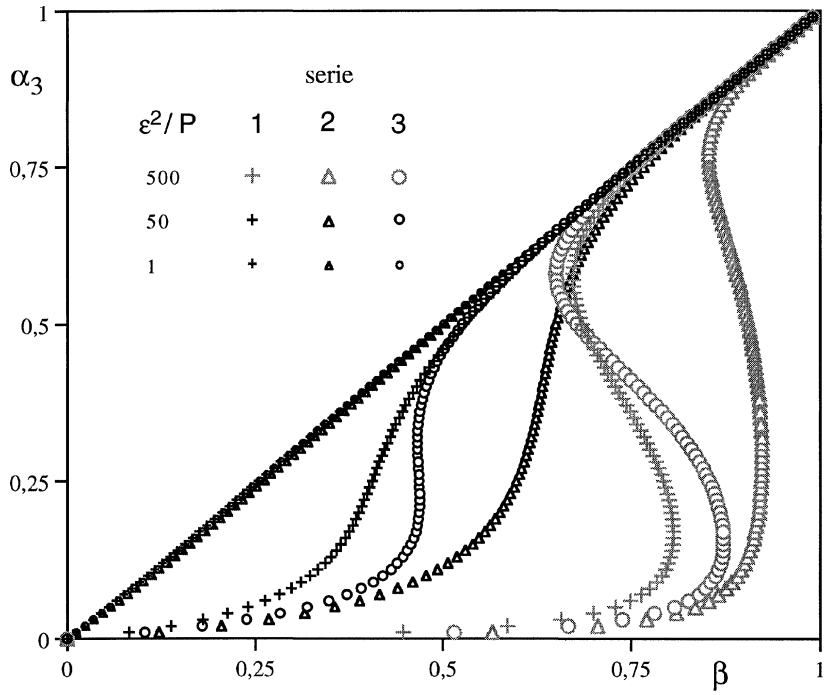

Figure 3. Void fraction in the core predicted by equation (37) for various hindering functions: Gal-Or and Waslo for contaminated bubbles ($\kappa = 6.27$, serie 1) and for clean bubbles ($\kappa = 0$, serie 2) and Richardson and Zaki (serie 3).

A condition for their appearence can be evaluated from equation (34) with $\tau_w = 0$ and equation (37), valid for the degenerate model. Then, zero friction occurs approximately when:

$$\beta \approx 1 - \frac{1 - \frac{6P}{\delta_1^*}}{1 + \frac{4}{3}\frac{\varepsilon^2}{\phi_1 \delta_1^*}\left(1 - \frac{6P}{\delta_1^*}\right)^2}. \tag{40}$$

Equation (40) reduces to $\beta = 6P/\delta_1^*$ with $\varepsilon^2 \ll 1$. The onset of secondary flows strongly depends on the single-phase layer width, which is not surprising. Indeed, as discussed in section 2.4.1, the flow field in this layer must compensate the increase of the liquid velocity (the increase concerned here is defined with respect to a single-phase situation) which occurs in the central zone due to its lower density. Since the width δ_1 is expected to change with flow conditions (and notably the bubble size), equation (40) is of little use without precise information on the void distribution. Such data have been collected over a limited set of parameters during the experiments mentioned at the beginning of section 3. Using δ_1^* determined from transverse void profiles (δ_1^* was found to be typically about 0.03), the prediction of equation (40) agrees well with the experimental frontier of secondary flows (*figure 4*). However, the comparison between measured and predicted liquid velocity profiles, given *figure 5*, is less satisfactory especially when back flow occurs, in which case their strength is underestimated. Indeed, predictions are based on $\delta_1^* = 0.03$, a value determined from void profiles obtained in upward flows. No such data have been collected when secondary flow occurs, and it is probable, as shown in *figure 5* by the prediction for $\delta_1^* = 0.06$, that the single-phase thickness increases once secondary flows take place.

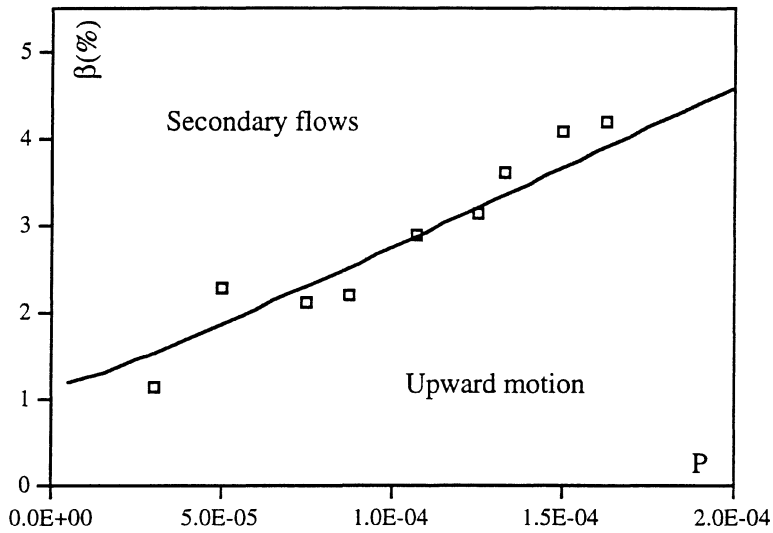

Figure 4. Onset of secondary flows; solid line: predictions from equation (40) with $\delta_1/e = 0.03$ and open squares: experimental results from Cartellier et al. [9].

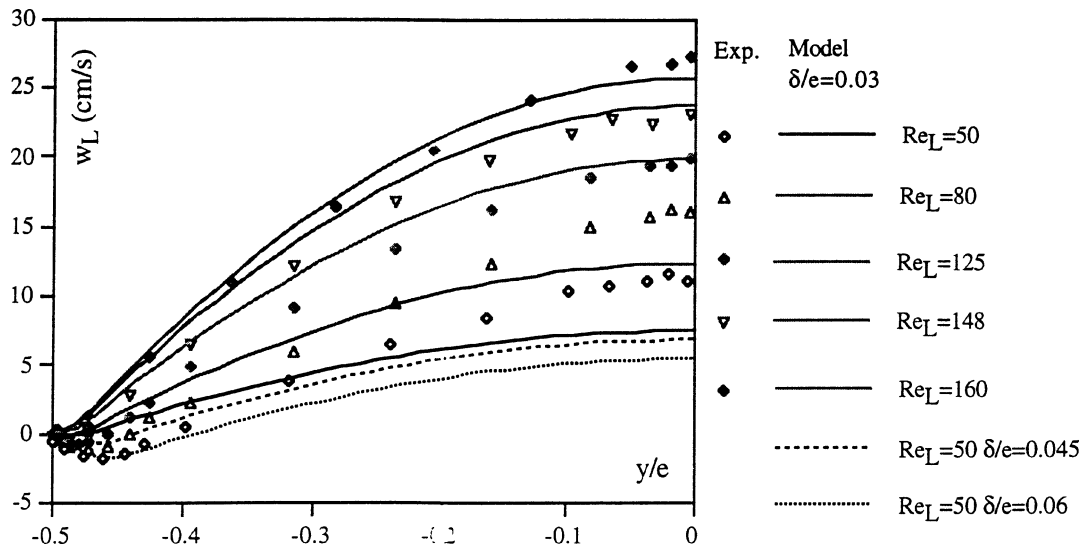

Figure 5. Comparison between experimental (Cartellier et al. [9]) and predicted liquid velocity profiles ($\beta = 0.02$, $\varepsilon = 0.011$, $\mathrm{Re_p} \in [1.4, 1.7]$, $K = 8.3$, ϕ_1 given by equation (39) with $\kappa = 6.27$).

3.3. Wall shear stress

To analyse the behaviour of the wall friction, let us start with the degenerated model. The wall shear stress given by equation (31), coupled with the lineic void fraction estimated via equation (37), furnishes an expression of τ_w function of the dimensionless characteristics parameters: the only unknown quantity left is the single phase layer thickness δ_1. Predicted trends are shown *figure 6* for the hindering function given by equation (39) and for $\varepsilon = 0.012$. First, τ_w/τ_{w0} tends asymptotically towards unity for large P whatever the gas content; this corresponds to flow conditions essentially governed by an equilibrium between the imposed

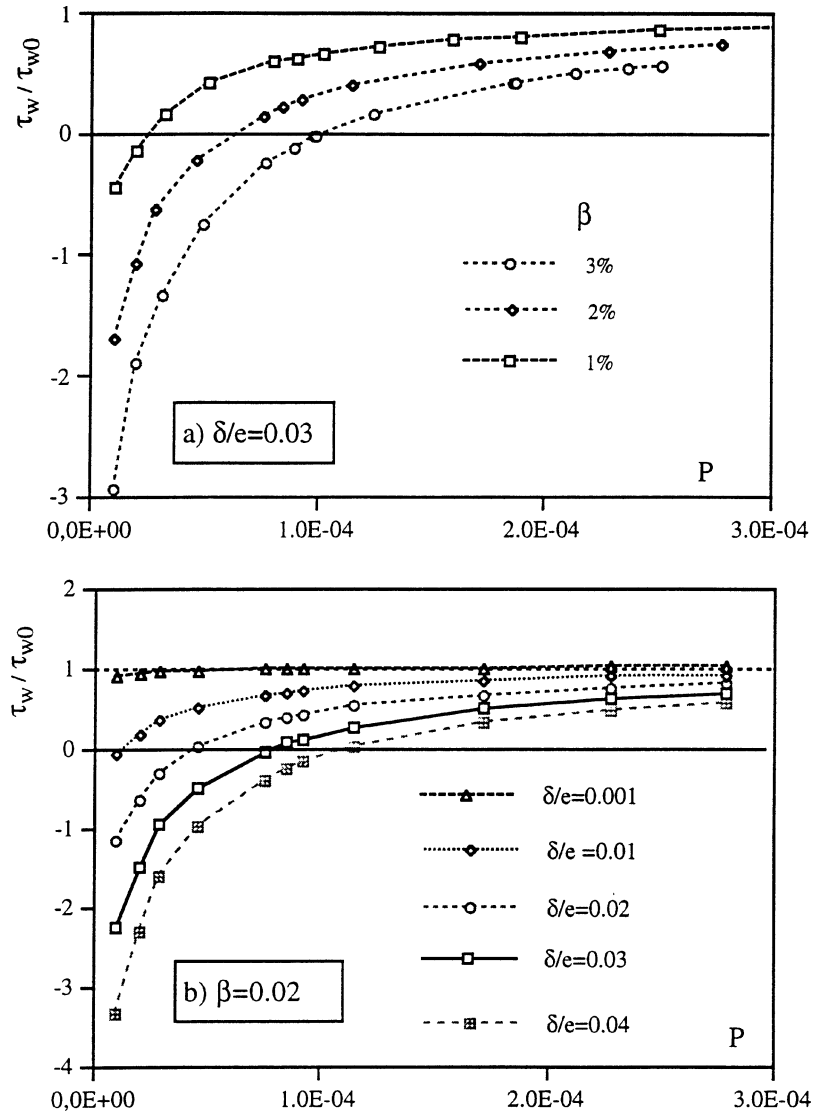

Figure 6. Wall shear stress ratio predicted by the degenerated model equation (34): influence of (a) the gas content and (b) the clear fluid layer thickness.

pressure gradient and the viscous stress in the continuous phase. On the other hand, for moderate or small P, the momentum exchange between phases contributes significantly to the liquid momentum balance equation, and the friction becomes also sensitive to the proportion of the dispersed phase, i.e. β, as shown by *figure 6(a)*. For fixed Poiseuille number P and gas flow rate ratio β, increasing the width of the clear fluid layer δ_1 causes a decrease (in algebraic value) of the wall shear stress as shown by *figure 6(b)*. In the limit of an homogeneous bubbly flow occupying the whole section of the duct ($\delta_1 = 0$), the ratio τ_w/τ_{w0} becomes $1/(1-\alpha)$ that is nearly unity at small gas content. Besides, provided that a clear fluid layer exists, the wall friction becomes positive ($\tau_w/\tau_{w0} < 0$) when P is low enough: such a limit has been discussed in the previous section. Most of these trends are in agreement with the experimental results, given *figure 7*, which have been obtained in plane Poiseuille bubbly flows (Moechti Triyogi [1]). This is notably the case for the Poiseuille number corresponding to zero crossing: indeed, for β in the range 1% to 3%, the zero shear stress is found experimentally for P

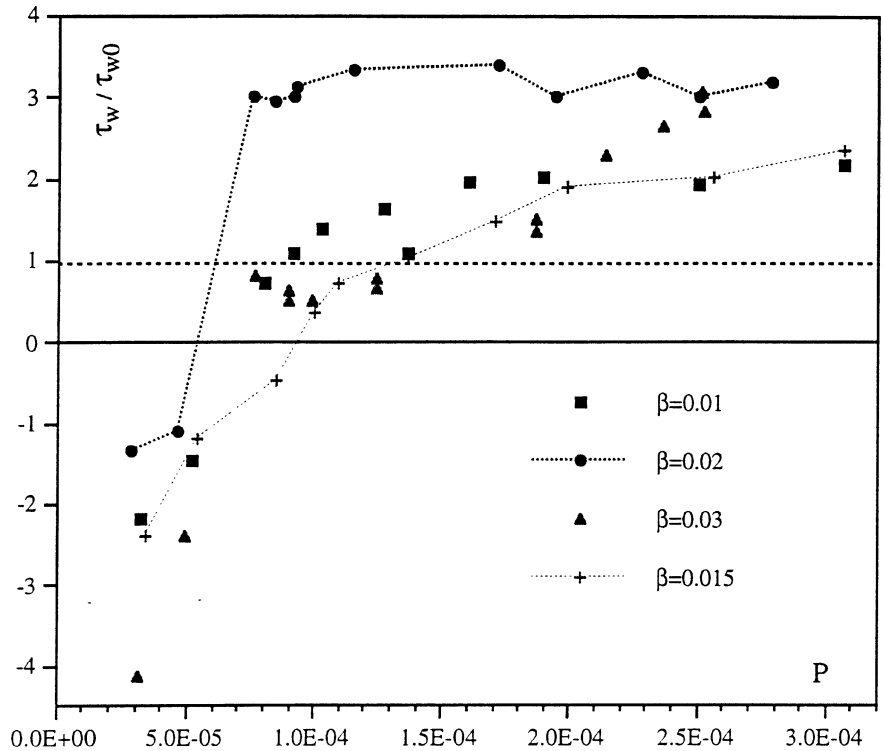

Figure 7. Experimental ratio of the wall friction in two-phase flow and in single-phase flow at the same liquid flow rate for various β ($\varepsilon \in [0.010, 0.013]$, $\mathrm{Re_p} \in [1.2, 1.9]$, $K = 8.3$, $\kappa = 6.27$).

in the interval $[3 \times 10^{-5}, 9 \times 10^{-5}]$, while the predicted P values pertain to $[2.5 \times 10^{-5}, 10^{-4}]$. The slight disagreement is probably due to an evolution of δ_1^* with flow conditions (see end of section 3.2) while the model has been exploited for a constant clear fluid layer thickness $\delta_1^* = 0.03$. Aside from these encouraging aspects, a major weakness of the degenerated model remains. Indeed, equation (34) is unable to provide ratios τ_w/τ_{w0} significantly higher than unity, in contradiction with the experimental findings of *figure 7*.

This drawback disappears when a more realistic void profile is taken into account because of the role of the excess gas, represented by $(a-1)(b-1)$ in equation (32). Predictions from equation (32) are given in *figure 8* where the characteristics of the void profile have been varied. Let us consider first the influence of the gas excess while maintaining δ_1 and α_3 constant (*figure 8(a)*). Again, as P increases, all curves tend toward an unit ratio for the same reasons as those evoked above. However, at low Poiseuille numbers, any value of the τ_w/τ_{w0} ratio can be obtained, depending on the parameter $(a-1)(b-1)$. High $(a-1)(b-1)$ means a large gas excess, or else a strong void peaking: the friction becomes much higher than its single-phase counterpart. Clearly, the two-phase layer increases the velocity in the near wall region and leads to a strong velocity gradient in the clear fluid layer. The ratio τ_w/τ_{w0} decreases as the amount of gas in the void peak does, but it remains higher than one until $(a-1)(b-1)$ equals unity, i.e. until the gas excess in the peak which equals $(\delta_2 - \delta_1)(\alpha_2 - \alpha_3)$ compensates the gas deficit $\alpha_3\delta_1$ of a degenerated model. This situation corresponds to $\langle\alpha\rangle$ equals α_3 (see equation (31) and comments thereafter). When wall peaking is weaker than the amount $\alpha_3\delta_1$, or when the void fraction in the zone 2 is less than or equal to that in the core ($b \leqslant 1$), the ratio τ_w/τ_{w0} becomes less than one, and one recovers the behaviour of the degenerated model, including the appearence of positive wall frictions ($\tau_w/\tau_{w0} < 0$). As expected from the role of density differences between layers, increasing the gas content produces an increase of the wall friction in absolute value whatever the void distribution (*figure 8(b)*). To analyse the influence of

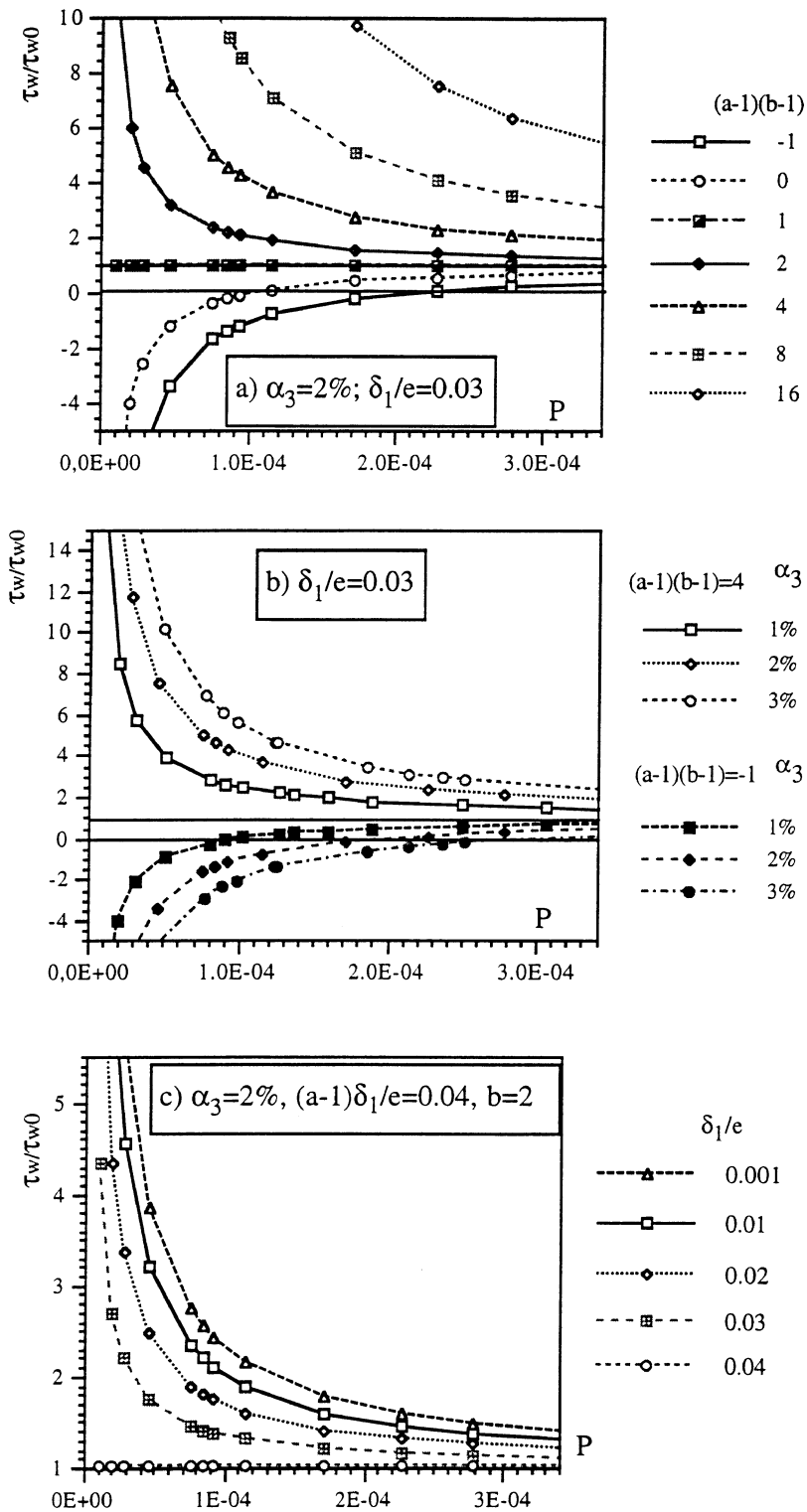

Figure 8. Wall shear stress ratio predicted by equation (32): influence of (a) the gas excess, of (b) the gas fraction and of (c) the clear fluid layer thickness.

the clear fluid layer, the width of the void peak and its amplitude have been maintained constant. As shown in *figure 8(c)*, the wall shear stress increases as the disturbing two-phase layer gets closer to the wall, and this holds in algebraic terms for any situation. All the modifications evoked above are clearly due to the higher velocity of the lighter two-fluid layers compared to that which would occur for the liquid alone.

When analysing a given experiment, not all of the ratios τ_w/τ_{w0} plotted, is *figure 8(a)* for example can be observed. The reason for this is simply that the parameters describing the idealised step function cannot vary freely. Instead, they result from transverse equilibria, and are thus expected to vary in some definite way, so that the corresponding wall shear stress have to jump from one curve to another in *figure 8*. To illustrate this, let us imagine an experiment for which all the dimensionless parameters are held fixed except the Poiseuille number. One would observe, for example, a flat void profile at low P, then the formation and the strengthening of void peaking, and at higher P, some flattening of the profile. In that case, τ_w/τ_{w0} will start at a negative value, then cross zero and grow above unity before decreasing while remaining positive. This scenario corresponds roughly to the measurements presented in *figure 7*.

Quantitative comparisons between calculated and experimental τ_w/τ_{w0} ratios have been undertaken whenever transverse void profiles and wall shear stress were simultaneously available. Among the data presented in *figure 7*, and which were obtained using an hot film probe flush mounted to the wall, only three of them can be used for the comparison. The corresponding void profiles are given in *figure 9*, and the first three lines of *table I* provide the parameters defining the idealised step-function as well as the measured and calculated wall friction ratio. Clearly, the predicted τ_w/τ_{w0} ratios follow the experimental trends, but with an underestimation of, at most 20%. This comparison can be considered as satisfactory partly owing to the reproducibility of friction measurements (about 10%) but mainly due to the lateral liquid velocity distribution which is not perfectly two-dimensional as required by the model. Indeed, the liquid flow rate per unit lateral length changes by an amount ranging from $\pm 8\%$ to $\pm 10\%$ along x, and friction measurements performed at $x = -15$ cm, 0 (center line of the channel) and 15 cm were found to evolve within $\pm 15\%$ (Moechti Triyogi [1]).

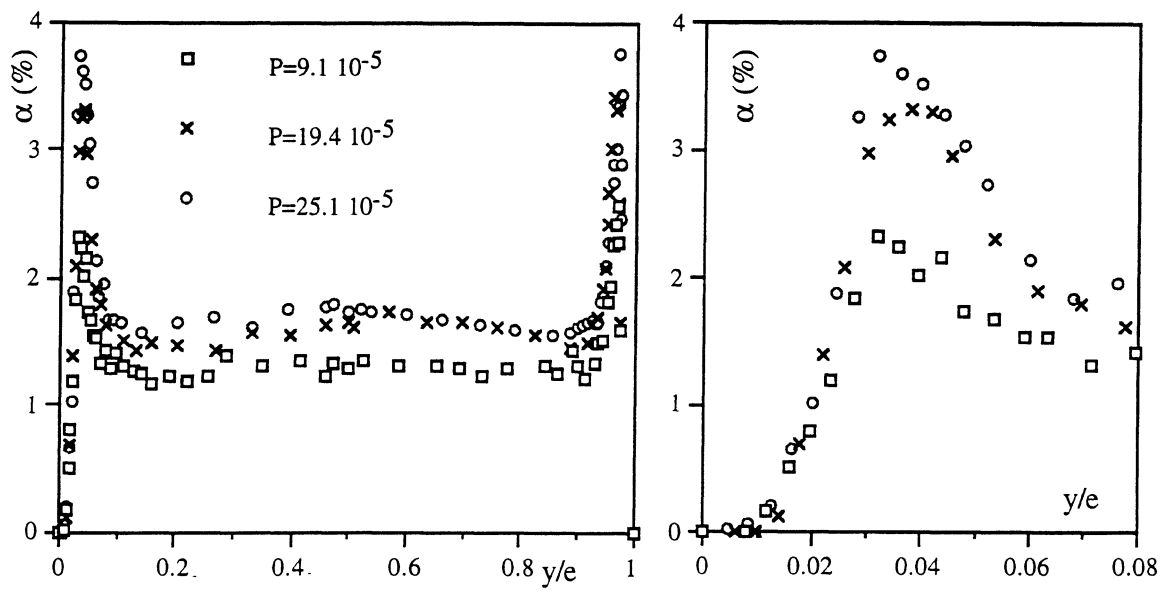

Figure 9. Experimental void fraction profiles for $\beta = 0.02$, $\varepsilon = 0.011$, $\mathrm{Re_p} = 1.5$. The wall region is enlarged on the right hand side (Moechti Triyogi [1]).

Table I. Comparison of calculated and measured wall friction ratio, where τ_{w0} is the single phase value at the same liquid flow rate.

Re_L	P	ε	β (%)	α_3 (%)	α_2 (%)	δ_1^*	δ_2^*	τ_w/τ_{w0} exp.	τ_w/τ_{w0} theor.
125	0.000091	0.011	2	1.25	2.4	0.010	0.095	3.0	2.68
300	0.000194	0.012	2	1.4	3.4	0.008	0.111	3.4	2.78
400	0.000251	0.012	2	1.6	3.9	0.008	0.111	3.2	2.59
200	0.000137	0.012	1	0.53	0.62	0.008	0.079	1.1	1.03

Additional data have been obtained recently in the same experimental set-up but with a slightly lower viscosity ($\rho_L = 1210$ kg/m^3, $\nu_L = 21.7 \times 10^{-6}$ m^2/s). The last line in *table I* corresponds to a rather flat void profile but still with a clear fluid layer of liquid near the wall. In that case, the wall friction has been deduced from the liquid velocity profiles (original data are given in Cartellier et al. [34]). The comparison between the prediction of equation (31) and the measurements is again satisfactory. A last check of the model is provided by a new type of flow structure obtained with bubbles with a mean diameter of 1.2 mm at very low gas content. Indeed, clusters composed of two or more bubbles appear for some flow conditions, and void coring occurs probably because of a change in the direction of the lift force (Cartellier et al. [34]). The example of void distribution given in *figure 10(a)* corresponds to $\beta = 1.4 \times 10^{-3}$, $P = 1.1 \times 10^{-4}$, or $Re_L = 300$, $\varepsilon = 0.019$, $\kappa = 6.27$ and to a particulate Reynolds number based on the actual relative velocity and on a single bubble diameter about 5. As shown by this example, the gas forms a curtain in the middle of the channel and the widths of the layers become here of the order of the channel thickness e. The complete model is thus required for the comparison. Setting $\phi_0 = (1-\alpha)^{-1}$, the axial liquid velocity profile can computed from equation (A1) using the definitions of s_1, s_2, s_3 (equations (22) and (23)) and the expressions of G (equation (25)), N (equation (30a)) and D (equation (30b)). As shown by *figure 10(b)*, the predicted axial liquid velocity profile agrees well with the experimental data. Similarly, the friction ratio predicted by equation (28) which equals 0.76, is within 12% of its experimental value deduced from the velocity profile. Hence, the proposed simplified model appears also valid for the case of multiple thick layers.

4. Conclusion

A simple model has been presented which gives access to the global features of plane Poiseuille bubbly flows. Instead of solving the transverse momentum balances, the void fraction distribution is imposed. Moreover, experimental void profiles are replaced by a step function which grasps all their important characteristics. Solving the axial momentum balances supplemented by closure laws provides all the variables and notably the velocity profiles, the lineic gas fraction and the wall shear stress. For the latter, simple analytical formula are derived which illustrate the mechanism in play, namely the differential buoyancy between layers which is responsible for the modification of the liquid velocity field. The influence of the layers position, width and associated void fraction have been analysed, and the essential role of the gas excess compared to an uniform gas distribution occupying the whole section has been underlined. All the important features experimentally observed are recovered, namely the appearance of downward secondary flows near walls and the fact that the wall friction in two-phase flow can be as large as many times its value in single-phase flow at the same liquid flow rate. The few quantitative comparisons also support the validity of the approach, even in the case of thick layers.

In practice, the proposed procedure can be used to estimate the wall friction starting from the void fraction profiles which are quite easy to measure. However, difficulties may occur concerning the fit of experimental profiles with a step function, and the sensitivity of the prediction to this procedure. Notably, a step function

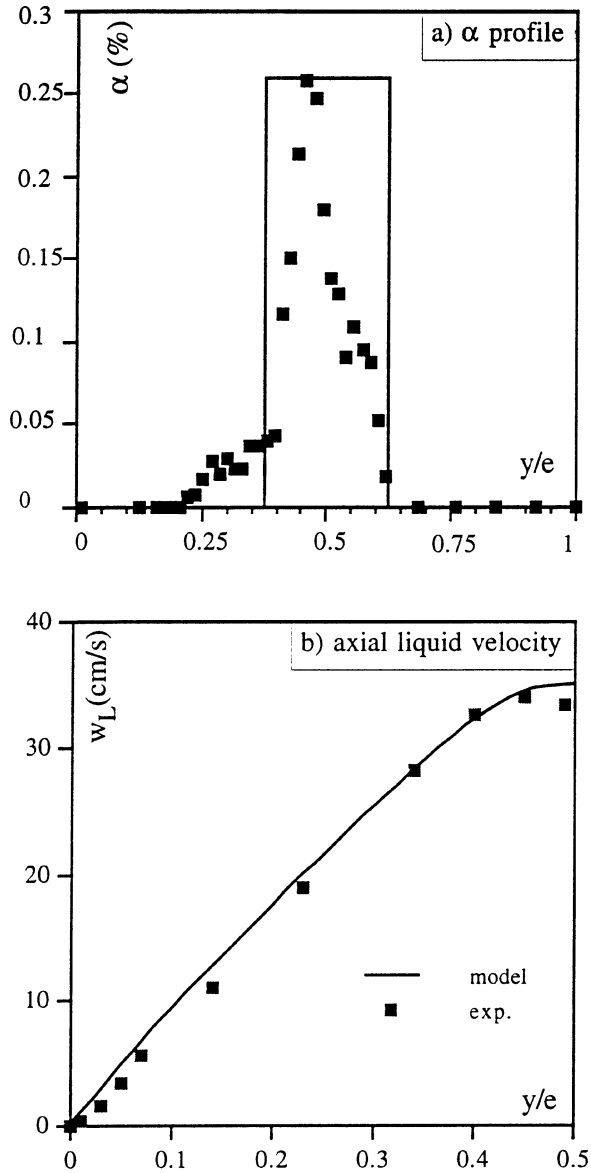

Figure 10. Bubble curtain in the center of the channel obtained with $\beta = 0.14\%$: (a) experimental void fraction profile, (b) axial liquid velocity as predicted by the full model (equations (A1)–(A3)) and as measured (Cartellier et al. [34]).

idealisation could be too crude when spatial gradients of the void fraction are not strong enough, in which case additional layers could be introduced. These questions will be touched upon in a companion paper devoted to quantitative comparisons between the model and experimental results.

Let us conclude with some words on the limits of the approach. It is clear that the assumption of parallel flows is invalidated when large scale instabilities occur, i.e. at high gas contents. Besides, neglecting the pseudo-turbulent stress compared to the viscous one is not a generally valid assumption, but the precise range of validity of this hypothesis is difficult to define unambiguously. Finally, the above model could be extended for the case of heavy particles provided that the momentum balance equation for the dispersed phase is revisited.

Acknowledgement

The authors would like to thanks J.L. Marié for fruitful discussions on the role of the void fraction structure in turbulent bubbly flows. Part of this work was performed under INTAS project 96-2319.

Appendix

The liquid axial velocity field deduced from equations (22) and (23) with the boundary conditions cited in the text becomes:

$$\begin{aligned} w_{\mathrm{L}}^{(1)}(y) &= s_1 y^2/2 + a_{11} y + a_{12}, \\ w_{\mathrm{L}}^{(2)}(y) &= s_2 y^2/2 + a_{21} y + a_{22}, \\ w_{\mathrm{L}}^{(3)}(y) &= s_3 y^2/2 + a_{31} y + a_{32}, \end{aligned} \tag{A1}$$

where the constant coefficients a_{ij} are:

$$\begin{aligned} a_{11} &= s_2(1-\alpha_2)\phi_0^{(2)}(\delta_1-\delta_2) - s_3(1-\alpha_3)\phi_0^{(3)}(e/2-\delta_2), \\ a_{12} &= 0, \\ a_{21} &= -s_2\delta_2 - s_3\frac{(1-\alpha_3)\phi_0^{(3)}}{(1-\alpha_2)\phi_0^{(2)}}(e/2-\delta_2), \\ a_{22} &= -s_1\delta_1^2/2 + \delta_1\left[1-(1-\alpha_2)\phi_0^{(2)}\right]\left[s_2(\delta_1-\delta_2) + s_3\frac{(1-\alpha_3)\phi_0^{(3)}}{(1-\alpha_2)\phi_0^{(2)}}(e/2-\delta_2)\right], \\ a_{31} &= -s_3 e/2, \\ a_{32} &= s_1\delta_1^{(2)}/2 + s_2\delta_1(\delta_1-\delta_2)\left[(1-\alpha_2)\phi_0^{(2)}-1\right] \\ &\quad + s_3\left[\delta_2(e/2-\delta_2)\left\{1-\frac{(1-\alpha_3)\phi_0^{(3)}}{(1-\alpha_2)\phi_0^{(2)}}\right\} + \delta_1(e/2-\delta_2)\left[(1-\alpha_2)\phi_0^{(2)}-1\right]\frac{(1-\alpha_3)\phi_0^{(3)}}{(1-\alpha_2)\phi_0^{(2)}} + \delta_2^2/2\right]. \end{aligned}$$

The factors N and D used in equation (25) become:

$$\begin{aligned} N = 1 &- 6\delta_2^*\left[1-\frac{(1-\alpha_3)\phi_0^{(3)}}{(1-\alpha_2)\phi_0^{(2)}}\right] - 6\delta_1^*\left[\frac{(1-\alpha_3)\phi_0^{(3)}}{(1-\alpha_2)\phi_0^{(2)}} - (1-\alpha_3)\phi_0^{(3)}\right] \\ &- 12\delta_1^{*2}\phi_0^{(3)}\left[1-2\alpha_2-\frac{1}{\phi_0^{(2)}}\right] - 24\delta_1^*\delta_2^*\phi_0^{(3)}\left[(\alpha_2-\alpha_3)\phi_0^{(3)} + \frac{\phi_0^{(3)}}{\phi_0^{(2)}} - \frac{(1-\alpha_3)\phi_0^{(3)}}{(1-\alpha_2)\phi_0^{(2)}}\right] \\ &- 12\delta_2^{*2}\left[\frac{2(1-\alpha_3)\phi_0^{(3)}}{(1-\alpha_2)\phi_0^{(2)}} - \frac{\phi_0^{(3)}}{\phi_0^{(2)}} - 1\right] - 24\delta_1^{*3}\frac{\phi_0^{(3)}}{1-\alpha_3}\left[\alpha_2(1-\alpha_2) + \frac{1-\alpha_2}{3\phi_0^{(2)}} - \frac{1}{3}\right] \\ &- 24\delta_1^{*2}\delta_2^*\frac{\phi_0^{(3)}}{1-\alpha_3}\left[(\alpha_2-\alpha_3)(2\alpha_2-1) + \frac{\alpha_2-\alpha_3}{\phi_0^{(2)}}\right] \\ &- 24\delta_1^*\delta_2^{*2}\frac{\phi_0^{(3)}}{1-\alpha_3}\left[-(\alpha_2-\alpha_3)^2 - \frac{2(1-\alpha_3)}{\phi_0^{(2)}} + \frac{1-\alpha_2}{\phi_0^{(2)}} + \frac{(1-\alpha_3)^2}{(1-\alpha_2)\phi_0^{(2)}}\right] \\ &- 24\delta_2^{*3}\frac{\phi_0^{(3)}}{1-\alpha_3}\left[-\frac{1-\alpha_2}{3\phi_0^{(2)}} + \frac{1-\alpha_3}{3\phi_0^{(3)}} + \frac{1-\alpha_3}{\phi_0^{(2)}} - \frac{(1-\alpha_3)^2}{(1-\alpha_2)\phi_0^{(2)}}\right], \end{aligned} \tag{A2}$$

$$
\begin{aligned}
D = 1 &- 6\delta_2^*\left[1 - \frac{(1-\alpha_3)\phi_0^{(3)}}{(1-\alpha_2)\phi_0^{(2)}}\right] - 6\delta_1^*\left[\frac{(1-\alpha_3)\phi_0^{(3)}}{(1-\alpha_2)\phi_0^{(2)}} - (1-\alpha_3)\phi_0^{(3)}\right] \\
&- 12\delta_1^{*2}\phi_0^{(3)}\left[\frac{1}{2}(1-\alpha_3)\phi_0^{(3)} + (1-\alpha_2)\phi_0^{(3)} - \frac{(1-\alpha_3)\phi_0^{(3)}}{2(1-\alpha_2)\phi_0^{(2)}} - \frac{\phi_0^{(3)}}{2} - \frac{\phi_0^{(3)}}{2\phi_0^{(2)}}\right] \\
&- 12\delta_1^*\delta_2^*\left[\frac{\phi_0^{(3)}}{\phi_0^{(2)}} + (1-\alpha_3)\phi_0^{(3)} - (1-\alpha_2)\phi_0^{(3)} - \frac{(1-\alpha_3)\phi_0^{(3)}}{(1-\alpha_2)\phi_0^{(2)}}\right] \\
&- 12\delta_2^{*2}\left[\frac{3}{2}\frac{(1-\alpha_3)\phi_0^{(3)}}{(1-\alpha_2)\phi_0^{(2)}} - \frac{\phi_0^{(3)}}{2\phi_0^{(2)}} - 1\right] - 24\delta_1^{*3}\phi_0^{(3)}\left[\frac{\phi_0^{(3)}}{6} - \frac{(1-\alpha_2)\phi_0^{(3)}}{2} + \frac{\phi_0^{(3)}}{3\phi_0^{(2)}}\right] \\
&- 24\delta_1^{*2}\delta_2^*\phi_0^{(3)}\left[\frac{(\alpha_3-\alpha_2)\phi_0^{(3)}}{2} - \frac{\phi_0^{(3)}}{2\phi_0^{(2)}} + \frac{(1-\alpha_3)\phi_0^{(3)}}{2(1-\alpha_2)\phi_0^{(2)}}\right] \\
&- 24\delta_1^*\delta_2^{*2}[0] - 24\delta_2^{*3}\left[\frac{1}{3} - \frac{(1-\alpha_3)\phi_0^{(3)}}{2(1-\alpha_2)\phi_0^{(2)}} + \frac{\phi_0^{(3)}}{6\phi_0^{(2)}}\right]. \qquad \text{(A3)}
\end{aligned}
$$

References

[1] Moechti Triyogi Y., Étude expérimentale des écoulements de Poiseuille à bulles plans. PhD, Institut National Polytechnique, Grenoble, 1993.

[2] Cartellier A., Moechti Triyogi Y., Achard J.L., Local variables in plane Poiseuille bubbly flows, in: Proc. 7th Workshop on Two-Phase Predictions, Erlangen, April 11–14, 1994.

[3] Valukina N., Koz'menko B., Kashinskii O., Characteristics of a flow of monodisperse gas-liquid mixture in a vertical tube, Inzhenerno-Fizicheskii Zhurnal 36 (1979) 695–699.

[4] Sato Y., Sadatomi M., Sekoguchi K., Momentum and heat transfer in two-phase bubble flow, Int. J. Multiphase Flow 7 (1981) 167–177 (part I) and 179–190 (part II).

[5] Nakoryakov V.E., Kashinsky O.N., Kozmenko B.K., Gorelik R.S., Investigation of upward bubbly flow at low liquid-phase velocity, Soviet Journal of Applied Physics 1 (3) (1987) 13–18.

[6] Kashinsky O., Timkin L., Cartellier A., Experimental study of "laminar" bubbly flows in a vertical pipe, Exp. in Fluids 14 (1993) 308–314.

[7] Rietema K., Ottengraf Ir., Laminar liquid circulation and bubble street formation in a gas-liquid system, Trans. Inst. Chem. Engrs. 48 (1970) T54–T62.

[8] Hills J.H., Radial non-uniformly of velocity and voidage in a bubble column, Trans. Inst. Chem. Engrs. 52 (1974) 1–9.

[9] Cartellier A., Moechti Triyogi Y., Achard J.L., Plane Poiseuille bubbly flows: void fraction and wall shear stress, in: Kelleher M.D. et al. (Eds), Experimental Heat Transfer and Thermodynamics, Elsevier Science Publishers, 1993, pp. 1402–1409.

[10] Cartellier A., Measurement of pseudo-turbulence in bubbly flows by phase Doppler anemometry, in: Proc. 7th Int. Symp. Applications of Laser Techniques to Fluid Mechanics, paper 31-5, Lisbon, Portugal, July 11–14, 1994.

[11] Kashinsky O., Timkin L., Cartellier A., Wall shear stress and velocity fluctuations in upward laminar bubbly flows, in: Celata G., Shah R. (Eds), Two-Phase Flow Modelling and Experimentation, Publ. Edizioni ETS, 1995, pp. 467–472.

[12] Celik I., Wang Y.Z., Numerical simulation of circulation in gas-liquid column reactors: isothermal, bubbly, laminar flow, Int. J. Multiphase Flow 20 (6) (1994) 1053–1070.

[13] Ishii M., Thermo-Fluid Dynamic Theory of Two-Phase Flow, Publ. Eyrolles, 1975.

[14] Achard J.L., Cartellier A., Local characteristics of upward laminar bubbly flows, PCH Physico Chemical Hydrodynamics 6 (5/6) (1985) 841–852.

[15] Zierep J., Über die kräfe und momente die auf einen tropfen in sherender strömung wirken, Z. F. Flugwiss 3 (1955) 22–25.

[16] Drew D., The plane Poiseuille flow of a particle-fluid mixture, J. Fluid Eng. 112 (1990) 362–366.

[17] Antal S.P., Lahey R.T. Jr., Flaherty J.E., Analysis of phase distribution in fully developed laminar bubbly two-phase flow, Int. J. Multiphase Flow 17 (5) (1991) 635–652.

[18] Wallis G.B., One Dimensional Two-Phase Flow, McGraw-Hill, 1969.

[19] Zuber N., Findlay J., Average volumetric concentration in two-phase flow systems, J. Heat Transfer (November 1965) 453–468.

[20] Clark N.N., Van Egmond J.W., Nebiolo E.P., The drift-flux model applied to bubble columns and low velocity flows, Int. J. Multiphase Flow 16 (2) (1990) 261–279.

[21] Moursali E., Marié J.L., Bataille J., An upward turbulent boundary layer along a vertical flat plate, Int. J. Multiphase Flow 21 (1) (1995) 107–117.

[22] Marié J.L., Moursali E., Trang-Cong S., Similarity law and turbulence intensity profiles in a bubbly boundary layer at low void fractions, Int. J. Multiphase Flow 23 (2) (1997) 227–247.
[23] Newman J., Retardation of falling drops, Chem. Eng. Sci. 22 (1967) 83–85.
[24] Ishii M., Zuber N., Drag coefficient and relative velocity in bubbly, droplet or particulate flows, AIChE J. 25 (5) (1979) 843–855.
[25] Achard J.L., Cartellier A., Rivière N., Two-fluid models and the representation of interaction terms in laminar dispersed two-phase flows at low concentration, in: Third International Conference on Multiphase Flow, ICMF'98, Lyon, France, June 8–12, 1998.
[26] Crispel S., Cartellier A., Simonin O., Achard J.L., Effet d'une paroi solide plane sur la densité de force interfaciale, paper 972, 14eme congrès français de mécanique, Toulouse, France, September 3–30, 1999.
[27] Joseph D.D., Lundgren T.S., Ensemble averaged and mixture theory equations for incompressible fluid-particle suspensions, Int. J. Multiphase Flow 16 (1990) 35–42.
[28] Achard J.L., Cartellier A., Extra deformation tensor in dispersed two-phase flow modelling, in: Proc. 5th Int. Symp. in Refined Flow Modelling and Turbulence Measurements, Ed. Presses E.N. Ponts et Chaussées, 1993, pp. 477–484.
[29] Ryskin G., The extensional viscosity of a dilute suspension of spherical particles at intermediate micro scale Reynolds numbers, J. Fluid Mech. 99 (3) (1980) 513–529 (with an appendix by Ryskin G. and Rallisson J.).
[30] Achard J.L., Cartellier A., Two-fluids models and the rheological approach of fluid-particle suspensions at low concentration, in: Euromech—3rd European Fluid Mechanics Conf., Göttingen, September 15–18, 1997.
[31] Nigmatulin R.I., Spatial averaging in the mechanics of heterogeneous and dispersed systems, Int. J. Multiphase Flow 5 (1979) 353–385.
[32] Biesheuvel R., Van Wijngaarden L., Two-phase flow equations for a dilute dispersion of gas bubbles in liquid, J. Fluid Mech. 148 (1984) 301–318.
[33] Cartellier A., Kashinsky O., Timkin L., Experimental characterisation of pseudo-turbulence in Poiseuille bubbly flows, in: Proc. 2nd Int. Conference on Multiphase Flow'95, Kyoto, 1995.
[34] Cartellier A., Timkin L., Rivière N., New structures of Poiseuille bubbly flows due to clustering, in: Proc. ASME FEDSM'97, paper 3528, Vancouver, June 22–26, 1997.
[35] Kashinsky O., Timkin L., Slip velocity measurements in upward bubbly flow by combined LDA and electrodiffusional technique, in: Modern Techniques and Measurements in Fluids Flows, Proc. 2nd Int. Conf. on Fluid Dynamics Measurements and Its Applications, Beijing, China, October 19–22, 1994, pp. 61–66.
[36] Zuber N., On the dispersed two-phase flow in the laminar regime, Chem. Eng. Sci. 19 (1964) 897–917.
[37] Richardson J.F., Zaki W.N., Sedimentation and fluidisation: Part I, Trans. Instn. Chem. Engrs. 32 (1954) 35–53.
[38] Gal-Or B., Waslo S., Hydrodynamics of an ensemble of drops (or bubbles) in the presence or the absence of surfactants, Chem. Eng. Sci. 23 (1968) 1431–1436.